



Article

Three-Dimensional Vanadium and Nitrogen Dual-Doped Ti_3C_2 Film with Ultra-High Specific Capacitance and High Volumetric Energy Density for Zinc-Ion Hybrid Capacitors

Xinhui Jin, Siliang Yue, Jiangcheng Zhang, Liang Qian and Xiaohui Guo *

Key Laboratory of Synthetic and Natural Functional Molecule Chemistry of Ministry of Education, The College of Chemistry and Materials Science, Northwest University, Xi'an 710069, China; jinxinhui@stumail.nwu.edu.cn (X.J.); yuesiliang98@163.com (S.Y.); zjc15433@163.com (J.Z.); 17613922518@163.com (L.Q.)

* Correspondence: guoxh2009@nwu.edu.cn

Abstract: Zinc-ion hybrid capacitors (ZICs) can achieve high energy and power density, ultralong cycle life, and a wide operating voltage window, and they are widely used in wearable devices, portable electronics devices, and other energy storage fields. The design of advanced ZICs with high specific capacity and energy density remains a challenge. In this work, a novel kind of V, N dual-doped Ti_3C_2 film with a three-dimensional (3D) porous structure (3D V-, N- Ti_3C_2) based on Zn-ion pre-intercalation can be fabricated via a simple synthetic process. The stable 3D structure and heteroatom doping provide abundant ion transport channels and numerous surface active sites. The prepared 3D V-, N- Ti_3C_2 film can deliver unexpectedly high specific capacitance of 855 F g^{-1} (309 mAh g^{-1}) and demonstrates 95.26% capacitance retention after 5000 charge/discharge cycles. In addition, the energy storage mechanism of 3D V-, N- Ti_3C_2 electrodes is the chemical adsorption of $\text{H}^+/\text{Zn}^{2+}$, which is confirmed by ex situ XRD and ex situ XPS. ZIC full cells with a competitive energy density (103 Wh kg^{-1}) consist of a 3D V-, N- Ti_3C_2 cathode and a zinc foil anode. The impressive results provide a feasible strategy for developing high-performance MXene-based energy storage devices in various energy-related fields.

Keywords: Ti_3C_2 ; doping; three-dimensional structure; hybrid supercapacitors; specific capacitance



Citation: Jin, X.; Yue, S.; Zhang, J.; Qian, L.; Guo, X. Three-Dimensional Vanadium and Nitrogen Dual-Doped Ti_3C_2 Film with Ultra-High Specific Capacitance and High Volumetric Energy Density for Zinc-Ion Hybrid Capacitors. *Nanomaterials* **2024**, *14*, 490. <https://doi.org/10.3390/nano14060490>

Academic Editors: Christian M. Julien and Jung Woo Lee

Received: 1 February 2024

Revised: 6 March 2024

Accepted: 6 March 2024

Published: 8 March 2024



Copyright: © 2024 by the authors. Licensee MDPI, Basel, Switzerland. This article is an open access article distributed under the terms and conditions of the Creative Commons Attribution (CC BY) license (<https://creativecommons.org/licenses/by/4.0/>).

1. Introduction

With the increasing demand for electronic devices and electric vehicles, various energy storage systems (e.g., lithium-ion batteries, supercapacitors, and metal-ion hybrid capacitors) with excellent electrochemical performance play an important role in modern society [1–12]. Among these, lithium-ion batteries have achieved extensive commercial application in various fields [13–16]. Nevertheless, the marketable applications of lithium-ion batteries are still limited by the availability and price of lithium metal and the safety problems of organic electrolytes. As a result, various metal-ion hybrid capacitors are widely favored for their ultralong cycle life, reliable safety, and high energy density [17–23]. In particular, zinc-ion capacitors (ZICs) are considered as potential energy storage devices because of the high theoretical specific capacity of their zinc anodes (820 mAh g^{-1} and 5854 mAh cm^{-3}), their environment-friendly nature, their robust stability, and their high level of safety [24–27].

Although ZICs exhibit good energy storage features compared to other conventional supercapacitors, some key technology parameters (e.g., low specific capacity and energy density) need to be further improved. The exploration of new cathode materials with high specific capacity and fast ion transport speed is urgently required [28–32]. At present, the cathode materials of ZICs mainly include carbon-based materials (activated carbon, hollow carbon spheres, and porous carbon) [33,34], TiN [35], conductive polymers [36], transition metal compounds [37], etc. However, the low specific capacity of these reported

cathode materials severely limits the energy density of ZICs. In an attempt to improve the energy storage performance of carbon-based materials, Yan et al. designed N-doped porous carbon with a capacity of 136.8 mAh g⁻¹ [38] for Zn//N-HPC zinc-ion devices with an extraordinary energy density (191 Wh kg⁻¹). Lu et al. fabricated ZICs with both ultra-high energy density (107.3 mAh g⁻¹) and excellent cycle lifetime (99.7% retention after 20,000 cycles) by utilising N-doped hierarchically porous carbon [39].

In recent years, an emerging two-dimensional material, MXene, has been investigated as an extremely promising cathode material for ZICs due to its intercalation pseudocapacitance mechanism, metallic-like conductivity, and variable surface modification [40–44]. The inevitable agglomerate stacking of MXene nanosheets reduces electrochemically active sites, limiting electrolyte ion diffusion, and prolongs the ion transport distance. To date, the aggregation and stacking problems of MXene have been solved by constructing a 3D structure, and the introduction of additional pseudocapacitance by heteroatom doping can improve MXene energy storage performance. For example, Zhang et al. demonstrated a 3D H-MXene hierarchical pore-structured film using H⁺ crosslinking. The specific capacity of the assembled Zn//3D-PHMF capacitor is 105 mAh g⁻¹ at 0.2 mA g⁻¹ [45]. Mateen et al. presented N-functionalization Ti₃C₂T_x in situ by means of hydrothermal reaction. The N-Ti₃C₂T_x exhibited an unrivalled specific capacitance of 583 F g⁻¹ at 1 A g⁻¹ [46]. N doping improved the surface wettability and electrical conductivity of MXene and greatly enhanced its electrochemical performance in supercapacitors. Gao et al. synthesized V-doped Ti₃C₂T_x using a hydrothermal method, which presented excellent specific capacitance (365.9 F g⁻¹) at 10 mV s⁻¹ and excellent stability of 95% (after 5000 cycles) [47]. Vanadium doping did not change the 2D morphology of MXene and resulted in stronger alkali metal-ion–O interactions on the MXene surface, introducing more active sites. Although these efforts have achieved the increased specific capacity of Ti₃C₂T_x, the relatively low specific capacity and low energy density have severely hindered the practical applications of Ti₃C₂ in ZICs.

Larger layer spacing can significantly increase the shuttle depth of electrolyte ions in Ti₃C₂, and ion pre-intercalation can expand the interlayer spacing, which is favorable for ion diffusion. Therefore, we present a kind of V, N dual-doped Ti₃C₂ film with a 3D porous structure (3D V-, N-Ti₃C₂) based on Zn²⁺ pre-intercalation via a three-step synthetic process involving HCl etching, hydrothermal doping, and Zn²⁺-induced gel. The prepared 3D V-, N-Ti₃C₂ film as a cathode displays an outstanding specific capacitance of ~855 F g⁻¹ (309 mAh g⁻¹) at 0.3 A g⁻¹ with an excellent cycling stability. Additionally, the assembled Zn//3D V-, N-Ti₃C₂ capacitors deliver an ultra-high energy density (103 Wh kg⁻¹), which is almost optimal compared with the currently reported ZICs. This work highlights the potential of the MXene-based materials in metal-ion capacitor systems and other energy storage fields.

2. Experimental Section

2.1. Preparation of Delaminated Ti₃C₂T_x

Delaminated Ti₃C₂T_x suspensions were produced from Ti₃AlC₂ powder using fluoride etching and an ultrasonic exfoliation process. Briefly, 1.6 g of LiF (Aladdin, 99%) was dissolved into 20 mL 9 M HCl and stirred for 5 min. Then, 1 g Ti₃AlC₂ powder was slowly added to the above mixed solution, and an oil bath at 60 °C was used for 48 h to remove Al from the Ti₃AlC₂ phase. The solution was then brought to room temperature and washed with deionized water using centrifugation until the pH was close to 7. After ultrasonic treatment under Ar for 2 h and centrifugation at 3500 rpm for 1 h, dark green supernatant was collected. The concentration of Ti₃C₂ was determined by drying a certain volume of the solution and weighing its mass.

2.2. Preparation of 3D V-, N-Ti₃C₂ Film

The 3D V-, N-Ti₃C₂ film was obtained via a hydrothermal method and freeze-drying process. Firstly, 20 mg Ti₃C₂ was dissolved in 10 mL DI water to obtain Ti₃C₂ suspension. Then, 2 g urea and 2 mg ammonium metavanadate (NH₄VO₃) was added into the Ti₃C₂

suspension; it was stirred for 15 min, and then transferred to a 15 mL Teflon-lined autoclave and maintained at 120 °C for 24 h. The solution was centrifuged and rinsed with deionized water several times. The V, N double-doped Ti_3C_2 film (V -, N - Ti_3C_2) was then obtained by vacuum filtration and vacuum drying. V -doped Ti_3C_2 film (V - Ti_3C_2) was prepared in the absence of urea according to the above procedure. Subsequently, 20 mg V -, N - Ti_3C_2 was dispersed into 20 mL deionized water and 0.6 mL ZnSO_4 (1 mg mL^{-1}) was added; the solution was then stirred for 4 h. The 3D V -, N - Ti_3C_2 film was obtained by means of vacuum filtration and freeze-drying. For comparison, 3D Ti_3C_2 film was also obtained by replacing V -, N - Ti_3C_2 with pure Ti_3C_2 .

2.3. Assembly of 3D V -, N - Ti_3C_2 // Zn Device

Typical 3D V -, N - Ti_3C_2 // Zn devices were constructed using sample 3D V -, N - Ti_3C_2 film as the cathode, Zn metallic sheet as the anode, and a glass fiber membrane as the separator. Here, 2 M ZnSO_4 was used as the electrolyte in the experiments.

3. Results and Discussion

The schematic fabrication process of 3D V -, N - Ti_3C_2 film is presented in Figure 1. Firstly, few-layered $\text{Ti}_3\text{C}_2\text{T}_x$ nanosheets were synthesized by etching Al from Ti_3AlC_2 in LiF and HCl mixed solution, and then ultrasonic exfoliation was performed, the SEM images of which are shown in Figure S1. Subsequently, the exfoliated Ti_3C_2 was then doped with V , N elements via the hydrothermal method in the presence of NH_4VO_3 and urea. V -, N - Ti_3C_2 was obtained by washing with deionized water. To increase the contact area, we added ZnSO_4 to V -, N - Ti_3C_2 suspension to enable Zn^{2+} ions to destroy the electrostatic repulsive forces between the nanosheets so as to link them together, forming a stable 3D structure. Subsequently, the 3D V -, N - Ti_3C_2 film was obtained using vacuum filtration and freeze-drying processes.

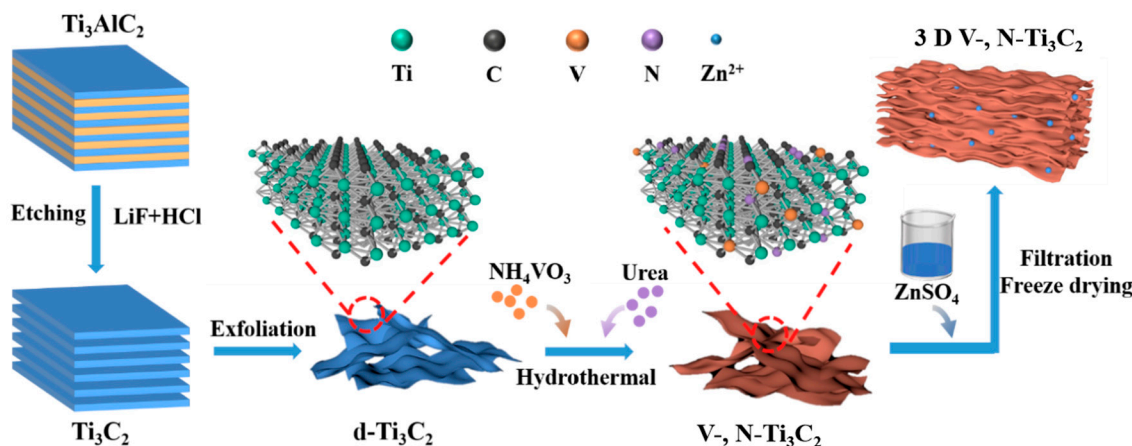


Figure 1. Schematic illustration of the synthesis process of the 3D V -, N - Ti_3C_2 film.

The XRD patterns of 3D V -, N - Ti_3C_2 and other samples are presented in Figures 2a and S1b. The Ti_3C_2 film has an intense (002) peak at around 6° , which confirms that Ti_3C_2 was successfully synthesized from Ti_3AlC_2 . The XRD pattern of 3D V -, N - Ti_3C_2 shows that the doping and structural design had minimal effect on Ti_3C_2 phase structure. The SEM images (Figures S1–S4 and 2b) showed the morphology of Ti_3C_2 film, 3D Ti_3C_2 film, V - Ti_3C_2 film, V -, N - Ti_3C_2 film, and 3D V -, N - Ti_3C_2 film. The SEM images of cross-sections of Ti_3C_2 film are shown in Figures S2 and S4a,b. V - Ti_3C_2 films and V -, N - Ti_3C_2 films show that the films are formed by the dense packing of Ti_3C_2 nanosheets. The V - Ti_3C_2 film and V -, N - Ti_3C_2 film are structurally dense and have small amounts of TiO_2 on the nanosheets' surface. The dense structure severely limits the exposure of surface active sites and ion diffusion, which in turn affects the electrochemical properties of the films. As for the 3D Ti_3C_2 film (the thickness is about 900 nm) and the 3D V -, N - Ti_3C_2 film (Figures 2b and S3),

stable 3D structures (the thickness is about 45 μm) are constructed by linking zinc ions (Zn^{2+}) and by using freeze-drying treatment. The stable 3D structure provides abundant ion channels for membrane electrodes, which dramatically improves their energy storage property. In addition, the nitrogen adsorption–desorption isotherms of V-, N- Ti_3C_2 , and 3D V-, N- Ti_3C_2 samples were of type I and type IV, respectively, as shown in Figure S5, indicating the presence of mesopores in V-, N- Ti_3C_2 and both micropores and mesopores in 3D V-, N- Ti_3C_2 . The surface areas of V-, N- Ti_3C_2 and 3D V-, N- Ti_3C_2 were 1.23 $\text{m}^2 \text{g}^{-1}$ and 45.17 $\text{m}^2 \text{g}^{-1}$, respectively. The 3D V-, N- Ti_3C_2 film had a larger specific surface area and provided abundant ion adsorption sites and transport channels. Then, TEM was used to observe the morphology and structure of 3D V-, N- Ti_3C_2 , as shown in Figure S6a. The 3D V-, N- Ti_3C_2 nanosheets were intertwined and connected with each other. The HRTEM image (Figure 2c) indicated that the crystal plane spacing of 3D V-, N- Ti_3C_2 was 1.23 nm, which was consistent with the (002) plane. The EDS elemental mapping analysis in Figure 2d confirms the coexistence of V, N, and Zn elements in the sample. The uniform distribution of these elements proves that V and N were successfully doped into Ti_3C_2 .

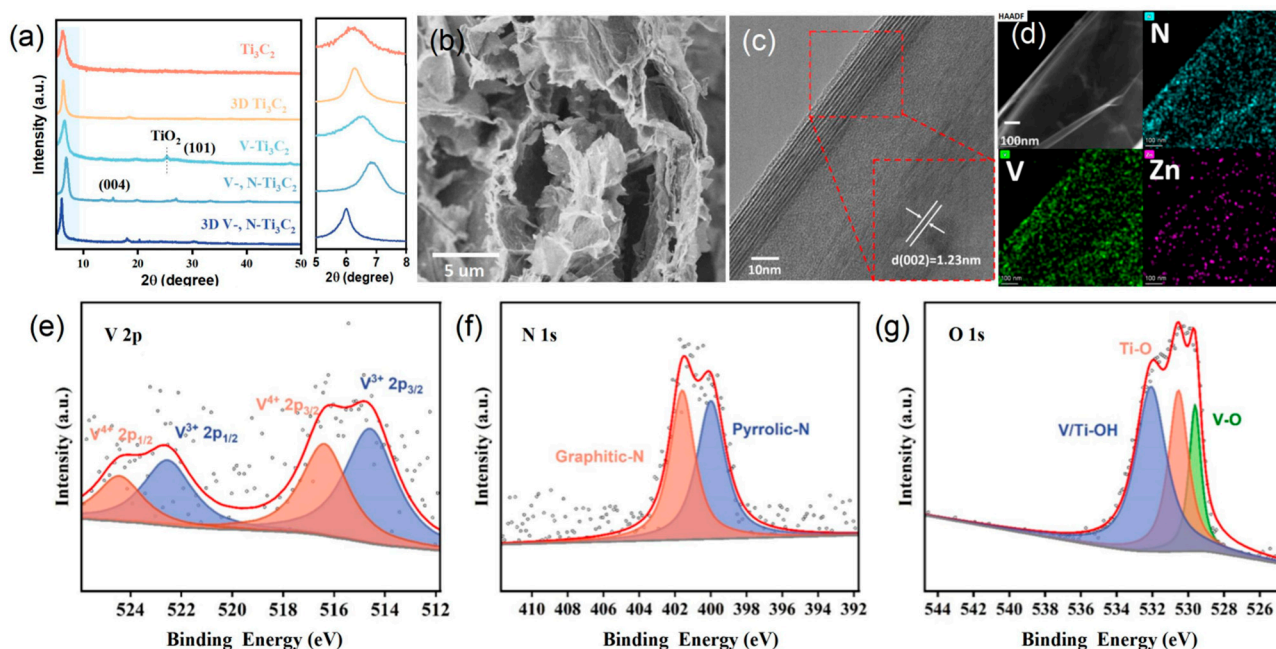


Figure 2. (a) XRD patterns of different Ti_3C_2 -based films. (b) Cross-sectional SEM image of the 3D V-, N- Ti_3C_2 film. (c) HRTEM image of 3D V-, N- Ti_3C_2 . (d) EDX elemental mapping of N, V, and Zn for the 3D V-, N- Ti_3C_2 . The XPS spectra of (e) V 2p, (f) N 1s, and (g) O 1s for the 3D V-, N- Ti_3C_2 film.

XPS was employed to investigate the elemental content and chemical state of 3D V-, N- Ti_3C_2 . The survey of XPS spectra and the high-resolution V 2p spectra of 3D V-, N- Ti_3C_2 are given in Figures S7 and 2e, respectively; they demonstrate the successful doping of V into Ti_3C_2 . The peaks at 516.4 and 524.5 eV correspond to $2p_{3/2}$ and $2p_{1/2}$ of V^{4+} , respectively [47]. The peaks at a binding energy of 514.6 and 522.5 eV are assigned to $2p_{3/2}$ and $2p_{1/2}$ of V^{3+} , respectively. The N 1s spectra are shown in Figure 2f, wherein the peaks at 400.0 and 401.6 eV correspond to pyrrolic-N and graphitic-N, respectively, indicating that N was successfully doped into Ti_3C_2 . [46,48,49]. Furthermore, a high-resolution O 1s spectrum can be simulated to synthesize three peaks; the peaks at 529.6, 530.5, and 532.1 eV correspond to O-V, O-Ti, and HO-V/Ti (Figure 2g), respectively [45]. The peak located at 282.0 eV in the C 1s spectrum (Figure S8b) can be attributed to the C-V, which provides evidence that V is successfully doped into Ti_3C_2 .

The Zn^{2+} storage properties of 3D V-, N- Ti_3C_2 and other electrode films were then investigated. Figure 3a displays the CV curves of Ti_3C_2 , 3D Ti_3C_2 , V- Ti_3C_2 , V-, N- Ti_3C_2 ,

and 3D V-, N-Ti₃C₂ at 0–1.3 V when the scanning rate was 5 mV s⁻¹. These CV curves have similar shapes, and there are some redox peaks (around 0.2–0.4 V and 0.7–1 V) during charge and discharge, indicating the reversible insertion/removal of Zn²⁺. However, under the same voltage window and scanning rate, the CV areas are in the order Ti₃C₂ < 3D Ti₃C₂ < V-Ti₃C₂ < V-, N-Ti₃C₂ < 3D V-, N-Ti₃C₂, which indicates that the capacity of 3D-structured MXene is higher than that of MXene film, and the optimal energy storage performance of 3D V-, N-Ti₃C₂ is mainly due to the rational creation of the 3D structure that can expand the contact area with the electrolyte ions and then expose more active sites. Additionally, the V-Ti₃C₂ and V-, N-Ti₃C₂ showed an improved electrochemical performance compared with that of Ti₃C₂; this is related to the dual-doping of V and N, which provide additional active sites. Figures S9–S13 show the CV curves of samples in 5–100 mV s⁻¹. With the increase in the scanning rate, the CV shape remains unchanged, indicating excellent high-speed and velocity performance. Figure 3b shows the GCD curves of the 3D V-, N-Ti₃C₂ at 0.3 to 20 A g⁻¹. Then, the GCD curves of Ti₃C₂, 3D Ti₃C₂, V-Ti₃C₂, and V-, N-Ti₃C₂ at different current density are shown in Figures S9–S12. The correlation between the gravimetric specific capacitance and current density for all the samples is given in Figure 3c. Similarly to the CV results, the 3D V-, N-Ti₃C₂ delivers the highest gravimetric capacitance at 0.3 A g⁻¹, up to 855 F g⁻¹ (309 mAh g⁻¹, Figure S13), and significantly more than the other samples. The gravimetric capacitance of 3D V-, N-Ti₃C₂ up to 122 F g⁻¹ at 15 A g⁻¹ is also better than that of the other electrodes and previously reported Ti₃C₂-based electrode materials (Table S1). Results demonstrate that a stable 3D structure can provide a larger active specific surface area and more ion transport channels, while the V, N dual-doping can provide more active sites for the improved capacitance. Remarkably, the 3D V-, N-Ti₃C₂ film electrode shows a maximum energy density of 200 Wh kg⁻¹ at a power density of 195 W Kg⁻¹ (Figure 3d), which is much higher than those of the previously reported zinc-ion capacitors [42,43,45,49]. Furthermore, the cycling stability of the 3D V-, N-Ti₃C₂ film electrode was tested at a current density of 8 A g⁻¹ (Figure 3e); 95.26% of its initial specific capacitance was retained after 5000 cycles, indicating robust long-term cycle stability. Figure S15 shows linear plots of the resultant charging current density and relevant scan rate for Ti₃C₂, 3D Ti₃C₂, V-Ti₃C₂, V-, N-Ti₃C₂, and 3D V-, N-Ti₃C₂, where the slopes are the electrochemical double layer capacitance (C_{dl}). The 3D V-, N-Ti₃C₂ with hierarchical holes had a large ECSA of 7.7 mF/cm², indicating that a large number of electrochemically active sites appeared in the material after V, N co-doping following Zn²⁺ pre-layering.

To analyse the kinetics of the charge storage of the 3D V-, N-Ti₃C₂ electrode, the CV curves of the 3D V-, N-Ti₃C₂ at 5–100 mV s⁻¹ are presented in Figure 4a. There is a pair of weak redox peaks on the CV curves, and the oxidation peaks (peak I) and reduction peaks (peak II) are gradually shifted towards the positive and negative directions with the increase in the scanning rate. The measured peak current (*i*) and scan rate (*v*) are measured based on the following relationship:

$$i = av^b \quad (1)$$

where *a* and *b* are variable parameters and *v* is the scan rate. The *b* value reflects the charge storage mechanism. If the *b* = 0.5, it is a diffusion-controlled process, whereas if the *b* = 1.0, the capacitor dominates the controlled process. The *b* value is the slope of linear fitting of log(*i*) versus log(*v*). As displayed in Figure 4b, the *b* value of peak I is 0.77, and of peak II it is 0.81, which suggests a hybrid capacitive and diffusion-controlled charge storage reaction mechanism.

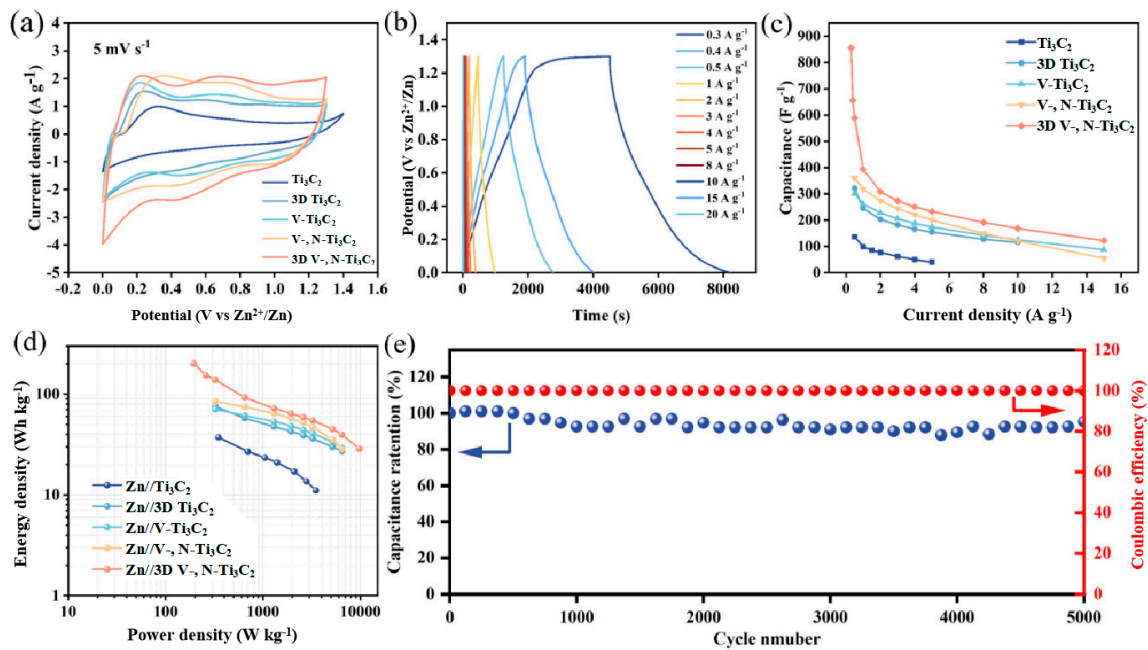


Figure 3. (a) CV curves of the Ti_3C_2 film, 3D Ti_3C_2 film, $\text{V-Ti}_3\text{C}_2$ film, $\text{V-, N-Ti}_3\text{C}_2$ film, and 3D $\text{V-, N-Ti}_3\text{C}_2$ film at 5 mV s^{-1} . (b) GCD curves of the 3D $\text{V-, N-Ti}_3\text{C}_2$ film electrode from 0.3 to 20 A g^{-1} . (c) Specific capacitance of all film electrodes at various current densities. (d) Energy and power density profiles for all film electrodes. (e) Cycling stability of the 3D $\text{V-, N-Ti}_3\text{C}_2$ film at 8 A g^{-1} .

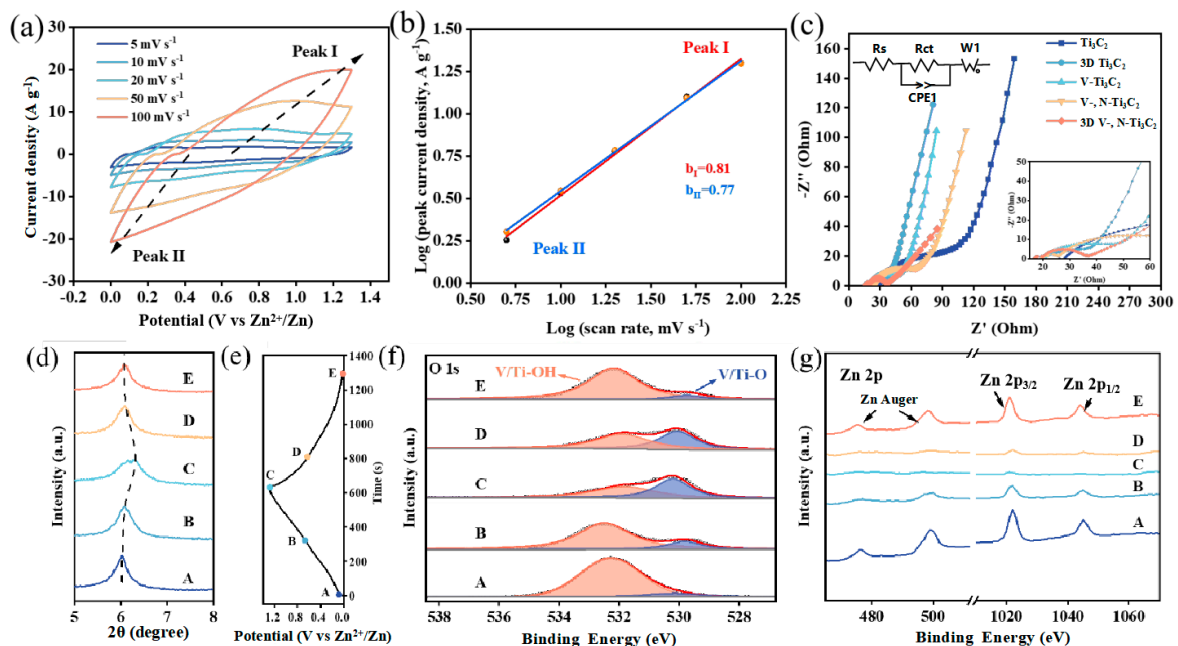


Figure 4. (a) CV curves of the 3D $\text{V-, N-Ti}_3\text{C}_2$ at 5 to 100 mV s^{-1} ; (b) the determination of the b values of the peak I and peak II based on $\log(i)$ versus $\log(v)$ plots; (c) Nyquist plots of 3D $\text{V-, N-Ti}_3\text{C}_2$ film, Ti_3C_2 film, 3D Ti_3C_2 film, $\text{V-Ti}_3\text{C}_2$ film, and $\text{V-, N-Ti}_3\text{C}_2$ film; (d) ex situ XRD patterns of the 3D $\text{V-, N-Ti}_3\text{C}_2$ cathode; (e) GCD profile of 3D $\text{V-, N-Ti}_3\text{C}_2$; (f) ex situ $\text{C } 1s$ XPS spectra of the 3D $\text{V-, N-Ti}_3\text{C}_2$ cathode; and (g) ex situ $\text{Zn } 2p$ XPS spectra of the 3D $\text{V-, N-Ti}_3\text{C}_2$ cathode.

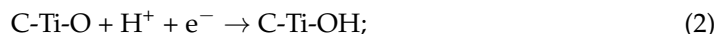
We further analysed the electrochemical kinetic processes with EIS (Figure 4c). The intercepts on the X-axis indicate the electron transfer resistances (R_s) in the high-frequency region. The R_s of Ti_3C_2 , 3D Ti_3C_2 , $\text{V-Ti}_3\text{C}_2$, $\text{V-, N-Ti}_3\text{C}_2$, and 3D $\text{V-, N-Ti}_3\text{C}_2$ are measured as

28.2, 20.6, 18.9, 19.3 and 16.5 Ω , respectively. After constructing the 3D structure, the R_s of 3D Ti_3C_2 and 3D V-, N- Ti_3C_2 are decreased to 19.3 and 16.5 Ω , respectively. This indicates that the 3D structure provides more ion transport channels and a larger specific surface area, which effectively reduce solution resistance and electrode resistance. Moreover, V- Ti_3C_2 and V-, N- Ti_3C_2 show smaller R_s values (18.9 and 19.3 Ω) than Ti_3C_2 (28.2 Ω), an indication of an enhancement of the conductivity of Ti_3C_2 by means of V, N dual-doping. The diameter of the semicircle on the X-axis exhibits charge transfer resistance (R_{ct}). The smaller R_{ct} of 3D V-, N- Ti_3C_2 (37.1 Ω) indicates that the 3D structure provides more charge transfer channels, while the V/N dual-doping effectively reduces the R_{ct} of Ti_3C_2 .

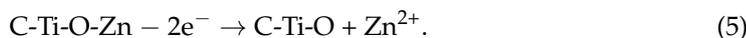
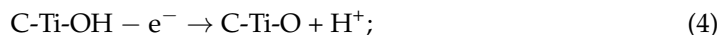
To understand the electrochemical reaction mechanism of the 3D V-, N- Ti_3C_2 cathode in ZIC devices, we further investigated the structural changes in 3D V-, N- Ti_3C_2 during charge–discharge processes by performing ex situ XRD and ex situ XPS. As shown in Figure 4e, based on the GCD curves of Zn//3D V-, N- Ti_3C_2 material and taking five representative locations (A, B, C, D, and E) of the cathode, we extracted the surface changes of samples under different charging/discharging conditions. The device was first charged from state A (0 V) to 1.3 V (state C) and then discharged to 0 V (state E) under a constant charging–discharging current. Figure 4d shows the XRD in different states. Firstly, when charging to 0.8 V from 0 V, the peak located at 6.02° indicated that the (002) plane of 3D V-, N- Ti_3C_2 experienced a small shift towards a higher angle at 6.07° . Continuing to charge from 0.8 V (state B) to 1.3 V, the (002) peak shifted significantly from 6.07° to 6.29° . This was mainly due to H^+/Zn^{2+} de-intercalation during the charging process, which caused a reduction in interlayer spacing. Furthermore, the (002) peak shifted from 6.29° to 6.09° with discharge from 1.3 to 0.8 V (state D), then, with discharge from 0.8 V to 0 V (state E), the (002) peak shifted from 6.09° to 6.05° . This was mainly caused by H^+/Zn^{2+} intercalation during the discharge process [50].

To capture more details of the reaction mechanism, the analysis was performed with ex situ XPS O 1s spectra (Figure 4f). The peaks at 532.6 and 531.6 eV at initial state belong to the V/Ti-OH and V/Ti-O groups, respectively. In the charge steps, the characteristic V/Ti-OH peak intensity at 532.6 eV undergoes a significant decrease from 0 to 0.8 V. As the charge process rises to 1.3 V, there is a slight decrease in the intensity of the characteristic peak of V/Ti-OH. In the discharge process, the intensity of the V/Ti-OH characteristic peak decreases slightly when the discharge voltage ranges from 1.3 V to 0.8 V, then manifests a sharp decrease following a further discharge to 0 V, which is related to the redox reaction of H^+ . To further investigate the contribution of Zn^{2+} in the charge/discharge process, the ex situ XPS Zn 2p spectra are shown in Figure 4g. Herein, the characteristic peak intensity of Zn 2p and the Auger lines of Zn decline in the charge process (from state A to state C) and then gradually increase during the discharge stage (from state C to state E). This phenomenon illustrates the electrochemical reaction of Zn^{2+} with the oxygen terminals on the surface of 3D V-, N- Ti_3C_2 during the charging–discharging process [42]. In general, the charge storage mechanism of 3D V-, N- Ti_3C_2 includes the pseudocapacitive behavior of H^+ and chemical absorption/desorption of Zn^{2+} . Based on ex situ XRD and XPS, the charge storage mechanism of the 3D V-, N- Ti_3C_2 cathode probably behaves as follows:

Discharge:



Charge:



To exemplify the viability of the 3D V-, N- Ti_3C_2 film for practical applications, ZIC devices were assembled with zinc sheet and 3D V-, N- Ti_3C_2 as anode and cathode, respectively (Figure 5a). The CV curves of the 3D V-, N- Ti_3C_2 //Zn show a rectangular shape with weak redox peaks at 5 mV s^{-1} to 100 mV s^{-1} in Figure 5b, indicating the

pseudo-capacitance feature of the 3D V-, N-Ti₃C₂//Zn ZIC. The GCD curves (Figure 5c) show symmetric charge/discharge processes at 0.5 to 10 A g⁻¹, implying a high coulombic efficiency. The specific capacitance and specific capacity were able to reach up to 441 F g⁻¹ and 159 mAh g⁻¹, respectively, at 0.5 A g⁻¹, implying an excellent energy storage performance (Figure 5d). Furthermore, we compared the energy density and power density of the 3D V-, N-Ti₃C₂//Zn with previously reported ZICs. As shown in Figure 5e, the 3D V-, N-Ti₃C₂//Zn ZIC 103 Wh kg⁻¹ energy density was at a power density of 325 W kg⁻¹, which was significantly superior to recently reported ZICs [29,34,45,46,51]. In addition, the 3D V-, N-Ti₃C₂//Zn ZIC full cells exhibited a favorable cyclic stability, which exhibited 86.6% capacity retention after 3000 cycles at 10 A g⁻¹ (Figure S14). To further verify the viability of the 3D V-, N-Ti₃C₂//Zn ZIC, we extended the working voltage window and capacity by connecting two ZIC devices in parallel and in series, as depicted in Figure 5b. As anticipated, the voltage window widened to 2.6 V when two devices were connected in series, and then two devices in parallel were able to double the capacity. A small red LED bulb was able to be successfully powered by two 3D V-, N-Ti₃C₂//Zn ZICs connected in series, indicating that the ZICs can work effectively in practical applications.

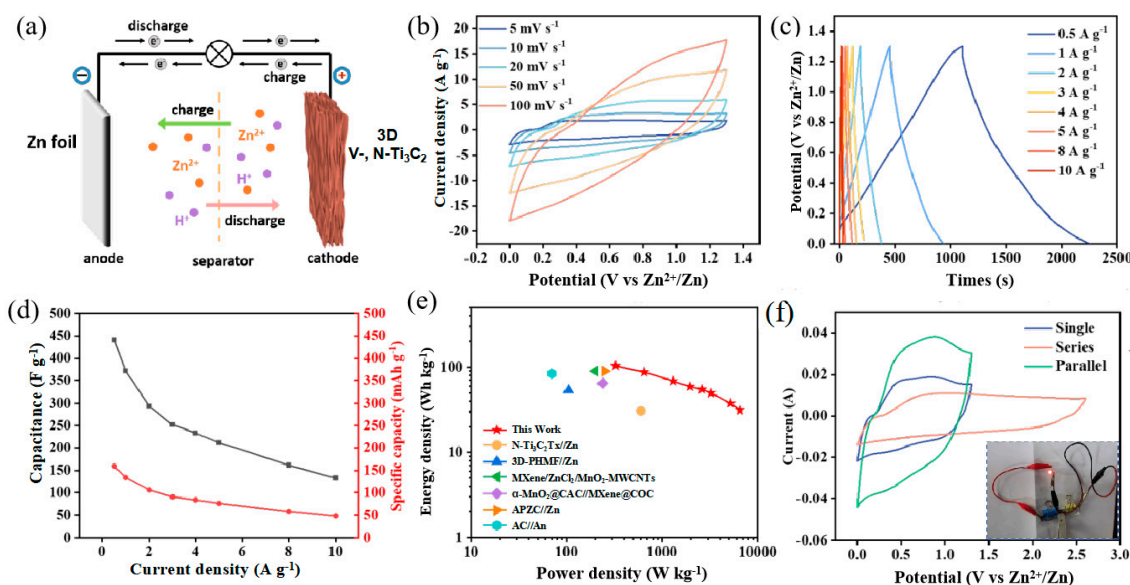


Figure 5. (a) Schematic diagram showing the discharging process of the 3D V-, N-Ti₃C₂//Zn ZIC. (b) CV curves of the 3D V-, N-Ti₃C₂//Zn ZIC from 5 to 100 mV s⁻¹. (c) GCD curves of 3D V-, N-Ti₃C₂//Zn ZIC at different current densities. (d) Specific capacity and specific capacitance of the 3D V-, N-Ti₃C₂//Zn ZIC. (e) Ragone plots of the 3D V-, N-Ti₃C₂//Zn ZIC in comparison with other reported ZICs. (f) CV curves of the two ZICs in series and parallel.

4. Conclusions

In summary, the 3D V-, N-Ti₃C₂ film electrode with a high specific capacity was rationally designed by constructing 3D structures and using V/N dual-doping. Thanks to the porous structure design, heteroatom doping, and metal-ion pre-intercalation, the fabricated 3D V-, N-Ti₃C₂ based on Zn-ion pre-intercalation delivered a maximum capacitance of 855 F g⁻¹ at 0.3 A g⁻¹ and demonstrated 95.26% capacitance retention after 5000 charge/discharge cycles. The dual-ion energy storage mechanism of H⁺/Zn²⁺ was revealed by using ex situ XRD and XPS. In addition, the as-assembled aqueous 3D V-, N-Ti₃C₂//Zn ZICs displayed 103 Wh kg⁻¹ energy density at a power density of 325 W kg⁻¹ and a favorable cycling durability. This work presents an illuminating insight into rational pore structural design and heteroatom doping to obtain a desirable specific capacity and energy density for MXene electrode materials in energy storage systems.

Supplementary Materials: The following supporting information can be downloaded at: <https://www.mdpi.com/article/10.3390/nano14060490/s1>, Figure S1. (a) SEM image few-layered $\text{Ti}_3\text{C}_2\text{T}_x$ nanosheets, (b) XRD of Ti_3AlC_2 and $\text{Ti}_3\text{C}_2\text{T}_x$. Figure S2. (a) SEM cross-sectional images, (b,c) the optical figures of Ti_3C_2 film. Figure S3. SEM cross-sectional images of 3D Ti_3C_2 film. Figure S4. SEM cross-sectional images of (a) V- Ti_3C_2 , (b) V-, N- Ti_3C_2 , and (c,d) 3D V-, N- Ti_3C_2 film. The inset is the optical figures of 3D V-, N- Ti_3C_2 film. Figure S5. N_2 adsorption–desorption isotherms of 3D V-, N- Ti_3C_2 and V-, N- Ti_3C_2 . Figure S6. (a) TEM images of the 3D V-, N- Ti_3C_2 , (b) EDX elemental mapping of Ti, O and C for the 3D V-, N- Ti_3C_2 . Figure S7. Survey XPS spectra of 3D V-, N- Ti_3C_2 film. Figure S8. High-resolution XPS spectra of (a) Ti 2p, (b) C 1s, (c) Zn 2p for the 3D V-, N- Ti_3C_2 film. Figure S9. (a) CV curves and (b) galvanostatic charge/discharge profiles of the Ti_3C_2 film. Figure S10. (a) CV curves and (b) galvanostatic charge/discharge profiles of the 3D Ti_3C_2 film. Figure S11. (a) CV curves and (b) galvanostatic charge/discharge profiles of the V- Ti_3C_2 film. Figure S12. (a) CV curves and (b) galvanostatic charge/discharge profiles of the V-, N- Ti_3C_2 film. Figure S13. Specific capacity and specific capacitance of the 3D V-, N- Ti_3C_2 film in 2M ZnSO_4 . Figure S14. Cycling performance of the 3D V-, N- Ti_3C_2 //Zn ZIC at 10 A g^{-1} . Figure S15. CV curves of the (a) Ti_3C_2 film, (b) 3D Ti_3C_2 film, (c) V- Ti_3C_2 film, (d) V-, N- Ti_3C_2 film, and (e) 3D V-, N- Ti_3C_2 film at different scanning rates, and (f) double-layer capacitance diagram of samples. Table S1. Comparison of storage energy performances between this work and previously reported in the literature. References [34,36,38,39,43,45,52] are cited in the Supplementary Materials.

Author Contributions: Methodology, S.Y. and L.Q.; Validation, J.Z.; Investigation, X.J.; Data curation, X.J., J.Z. and L.Q.; Writing—original draft, S.Y.; Writing—review & editing, X.J. and X.G.; Visualization, X.G.; Supervision, X.G. All authors have read and agreed to the published version of the manuscript.

Funding: This work was supported by the key projects of intergovernmental international cooperation in key R&D programs of the Ministry of Science and Technology of China (No. 2021YFE0115800), and by the National Science Funding Committee of China (No. U20A20250).

Data Availability Statement: Data are contained within the article and Supplementary Materials.

Conflicts of Interest: The authors declare no conflicts of interest.

References

1. Zeng, X.; Li, M.; Abd El-Hady, D.; Alshitari, W.; Al-Bogami, A.S.; Lu, J.; Amine, K. Commercialization of lithium battery technologies for electric vehicles. *Adv. Energy Mater.* **2019**, *9*, 1900161. [CrossRef]
2. Wang, X.; Wang, M.; Zhang, X.; Li, H.; Guo, X. Low-cost, green synthesis of highly porous carbons derived from lotus root shell as superior performance electrode materials in supercapacitor. *J. Energy Chem.* **2016**, *25*, 26–34. [CrossRef]
3. Harper, G.; Sommerville, R.; Kendrick, E.; Driscoll, L.; Slater, P.; Stolkin, R.; Walton, A.; Christensen, P.; Heidrich, O.; Lambert, S.; et al. Recycling lithium-ion batteries from electric vehicles. *Nature* **2019**, *575*, 75–86. [CrossRef] [PubMed]
4. Sunku Prasad, J.; Muthukumar, P.; Desai, F.; Basu, D.N.; Rahman, M.M. A critical review of high-temperature reversible thermochemical energy storage systems. *Appl. Energy* **2019**, *254*, 113733. [CrossRef]
5. Zhu, R.; Duan, H.; Zhao, Z.; Pang, H. Recent progress of dimensionally designed electrode nanomaterials in aqueous electrochemical energy storage. *J. Mater. Chem. A* **2021**, *9*, 9535–9572. [CrossRef]
6. Hager, M.D.; Esser, B.; Feng, X.; Schuhmann, W.; Theato, P.; Schubert, U.S. Polymer-based batteries-flexible and thin energy storage systems. *Adv. Mater.* **2020**, *32*, 2000587. [CrossRef] [PubMed]
7. Satpathy, S.; Das, S.; Bhattacharyya, B.K. How and where to use super-capacitors effectively, an integration of review of past and new characterization works on super-capacitors. *J. Energy Storage* **2020**, *27*, 101044. [CrossRef]
8. Zhang, L.; Li, X.; Yang, M.; Chen, W. High-safety separators for lithium-ion batteries and sodium-ion batteries: Advances and perspective. *Energy Storage Mater.* **2021**, *41*, 522–545. [CrossRef]
9. Yan, J.; Li, S.; Lan, B.; Wu, Y.; Lee, P.S. Rational design of nanostructured electrode materials toward multifunctional supercapacitors. *Adv. Funct. Mater.* **2019**, *30*, 1902564. [CrossRef]
10. Dong, L.; Yang, W.; Yang, W.; Li, Y.; Wu, W.; Wang, G. Multivalent metal ion hybrid capacitors: A review with a focus on zinc-ion hybrid capacitors. *J. Mater. Chem. A* **2019**, *7*, 13810–13832. [CrossRef]
11. Dong, S.; Lv, N.; Wu, Y.; Zhu, G.; Dong, X. Lithium-ion and sodium-ion hybrid capacitors: From insertion-type materials design to devices construction. *Adv. Funct. Mater.* **2021**, *31*, 2100455. [CrossRef]
12. Liu, S.; Kang, L.; Zhang, J.; Jun, S.C.; Yamauchi, Y. Carbonaceous anode materials for non-aqueous sodium-and potassium-ion hybrid capacitors. *ACS Energy Lett.* **2021**, *6*, 4127–4154. [CrossRef]
13. Chen, L.; Cao, L.; Ji, X.; Hou, S.; Li, Q.; Chen, J.; Yang, C.; Eidson, N.; Wang, C. Enabling safe aqueous lithium ion open batteries by suppressing oxygen reduction reaction. *Nat. Commun.* **2020**, *11*, 2638. [CrossRef]

14. Galos, J.; Pattarakunnan, K.; Best, A.S.; Kyratzis, I.L.; Wang, C.H.; Mouritz, A.P. Energy Storage Structural Composites with Integrated Lithium-Ion Batteries: A Review. *Adv. Mater. Technol.* **2021**, *6*, 2001059. [[CrossRef](#)]
15. Lu, M.; Zhang, X.; Ji, J.; Xu, X.; Zhang, Y. Research progress on power battery cooling technology for electric vehicles. *J. Energy Storage* **2020**, *27*, 101155. [[CrossRef](#)]
16. Chen, H.; Zhang, T.; Gao, Q.; Han, Z.; Xu, Y.; Yang, K.; Xu, X.; Liu, X. Advance and prospect of power battery thermal management based on phase change and boiling heat transfer. *J. Energy Storage* **2022**, *53*, 105254. [[CrossRef](#)]
17. Liu, X.; Sun, Y.; Tong, Y.; Wang, X.; Zheng, J.; Wu, Y.; Li, H.; Niu, L.; Hou, Y. Exploration in materials, electrolytes and performance towards metal ion (Li, Na, K, Zn and Mg)-based hybrid capacitors: A review. *Nano Energy* **2021**, *86*, 106070. [[CrossRef](#)]
18. Zhang, Y.; Wang, Z.; Li, D.; Sun, Q.; Lai, K.; Li, K.; Yuan, Q.; Liu, X.; Ci, L. Ultrathin carbon nanosheets for highly efficient capacitive K-ion and Zn-ion storage. *J. Mater. Chem. A* **2020**, *8*, 22874–22885. [[CrossRef](#)]
19. Divya, M.L.; Lee, Y.-S.; Aravindan, V. Solvent Co-intercalation: An Emerging Mechanism in Li-, Na-, and K-Ion Capacitors. *ACS Energy Lett.* **2021**, *6*, 4228–4244. [[CrossRef](#)]
20. Wu, M.; Zheng, W.; Hu, X.; Zhan, F.; He, Q.; Wang, H.; Zhang, Q.; Chen, L. Exploring 2D Energy Storage Materials: Advances in Structure, Synthesis, Optimization Strategies, and Applications for Monovalent and Multivalent Metal-Ion Hybrid Capacitors. *Small* **2022**, *18*, 2205101. [[CrossRef](#)]
21. Gong, X.; Chen, J.; Lee, P.S. Zinc-Ion Hybrid Supercapacitors: Progress and Future Perspective. *Batter. Supercaps* **2021**, *4*, 1529–1546. [[CrossRef](#)]
22. Minakshi, M.; Wickramaarachchi, K. Electrochemical aspects of supercapacitors in perspective: From electrochemical configurations to electrode materials processing. *Prog. Solid State Chem.* **2023**, *69*, 100390. [[CrossRef](#)]
23. Wickramaarachchi, K.; Sundaram, M.M.; Henry, D.J.; Gao, X. Alginate Biopolymer Effect on the Electrodeposition of Manganese Dioxide on Electrodes for Supercapacitors. *ACS Appl. Energy Mater.* **2021**, *4*, 7040–7051. [[CrossRef](#)]
24. Dong, L.; Yang, W.; Yang, W.; Tian, H.; Huang, Y.; Wang, X.; Xu, C.; Wang, C.; Kang, F.; Wang, G. Flexible and conductive scaffold-stabilized zinc metal anodes for ultralong-life zinc-ion batteries and zinc-ion hybrid capacitors. *Chem. Eng. J.* **2020**, *384*, 123355. [[CrossRef](#)]
25. Tang, H.; Yao, J.; Zhu, Y. Recent developments and future prospects for zinc-ion hybrid capacitors: A review. *Adv. Energy Mater.* **2021**, *11*, 2003994. [[CrossRef](#)]
26. Zhang, X.; Pei, Z.; Wang, C.; Yuan, Z.; Wei, L.; Pan, Y.; Mahmood, A.; Shao, Q.; Chen, Y. Flexible zinc-ion hybrid fiber capacitors with ultrahigh energy density and long cycling life for wearable electronics. *Small* **2019**, *15*, 1903817. [[CrossRef](#)] [[PubMed](#)]
27. Guo, Q.; Han, Y.; Chen, N.; Qu, L. Few-layer siloxene as an electrode for superior high-rate zinc ion hybrid capacitors. *ACS Energy Lett.* **2021**, *6*, 1786–1794. [[CrossRef](#)]
28. Guo, Q.; Liu, J.; Bai, C.; Chen, N.; Qu, L. 2D Silicene Nanosheets for High-Performance Zinc-Ion Hybrid Capacitor Application. *ACS Nano* **2021**, *15*, 16533–16541. [[CrossRef](#)]
29. Shi, J.; Wang, S.; Wang, Q.; Chen, X.; Du, X.; Wang, M.; Zhao, Y.; Dong, C.; Ruan, L.; Zeng, W. A new flexible zinc-ion capacitor based on δ -MnO₂@ Carbon cloth battery-type cathode and MXene@ Cotton cloth capacitor-type anode. *J. Power Sources* **2020**, *446*, 227345. [[CrossRef](#)]
30. Li, J.; Zhang, J.; Yu, L.; Gao, J.; He, X.; Liu, H.; Guo, Y.; Zhang, G. Dual-doped carbon hollow nanospheres achieve boosted pseudocapacitive energy storage for aqueous zinc ion hybrid capacitors. *Energy Storage Mater.* **2021**, *42*, 705–714. [[CrossRef](#)]
31. Zhang, L.; Liu, Z.; Wang, G.; Feng, J.; Ma, Q. Developing high voltage Zn (TFSI)₂/Pyr₁₄TFSI/AN hybrid electrolyte for a carbon-based Zn-ion hybrid capacitor. *Nanoscale* **2021**, *13*, 17068–17076. [[CrossRef](#)] [[PubMed](#)]
32. Zeng, J.; Dong, L.; Sun, L.; Wang, W.; Zhou, Y.; Wei, L.; Guo, X. Printable zinc-ion hybrid micro-capacitors for flexible self-powered integrated units. *Nano-Micro Lett.* **2020**, *13*, 19. [[CrossRef](#)] [[PubMed](#)]
33. Wang, D.; Pan, Z.; Lu, Z. From starch to porous carbon nanosheets: Promising cathodes for high-performance aqueous Zn-ion hybrid supercapacitors. *Micropor. Mesopor. Mat.* **2020**, *306*, 110445. [[CrossRef](#)]
34. Dong, L.; Ma, X.; Li, Y.; Zhao, L.; Liu, W.; Cheng, J.; Xu, C.; Li, B.; Yang, Q.-H.; Kang, F. Extremely safe, high-rate and ultralong-life zinc-ion hybrid supercapacitors. *Energy Storage Mater.* **2018**, *13*, 96–102. [[CrossRef](#)]
35. Huang, Z.; Wang, T.; Song, H.; Li, X.; Liang, G.; Wang, D.; Yang, Q.; Chen, Z.; Ma, L.; Liu, Z.; et al. Effects of Anion Carriers on Capacitance and Self-Discharge Behaviors of Zinc Ion Capacitors. *Angew. Chem.* **2020**, *60*, 1011–1021. [[CrossRef](#)] [[PubMed](#)]
36. Han, J.; Wang, K.; Liu, W.; Li, C.; Sun, X.; Zhang, X.; An, Y.; Yi, S.; Ma, Y. Rational design of nano-architecture composite hydrogel electrode towards high performance Zn-ion hybrid cell. *Nanoscale* **2018**, *10*, 13083–13091. [[CrossRef](#)] [[PubMed](#)]
37. Wang, S.; Wang, Q.; Zeng, W.; Wang, M.; Ruan, L.; Ma, Y. A new free-standing aqueous zinc-ion capacitor based on MnO₂-CNTs cathode and MXene anode. *Nano-Micro Lett.* **2019**, *11*, 70. [[CrossRef](#)]
38. Liu, P.; Gao, Y.; Tan, Y.; Liu, W.; Huang, Y.; Yan, J.; Liu, K. Rational design of nitrogen doped hierarchical porous carbon for optimized zinc-ion hybrid supercapacitors. *Nano Res.* **2019**, *12*, 2835–2841. [[CrossRef](#)]
39. Zhang, H.; Liu, Q.; Fang, Y.; Teng, C.; Liu, X.; Fang, P.; Tong, Y.; Lu, X. Boosting Zn-ion energy storage capability of hierarchically porous carbon by promoting chemical adsorption. *Adv. Mater.* **2019**, *31*, e1904948. [[CrossRef](#)]
40. Peng, M.; Wang, L.; Li, L.; Tang, X.; Huang, B.; Hu, T.; Yuan, K.; Chen, Y. Manipulating the Interlayer Spacing of 3D MXenes with Improved Stability and Zinc-Ion Storage Capability. *Adv. Funct. Mater.* **2021**, *32*, 2109524. [[CrossRef](#)]

41. Li, X.; Li, M.; Yang, Q.; Wang, D.; Ma, L.; Liang, G.; Huang, Z.; Dong, B.; Huang, Q.; Zhi, C. Vertically aligned Sn⁴⁺ preintercalated Ti₂CT_x MXene sphere with enhanced Zn ion transportation and superior cycle lifespan. *Adv. Energy Mater.* **2020**, *10*, 2001394. [[CrossRef](#)]
42. Cao, Z.; Fu, J.; Wu, M.; Hua, T.; Hu, H. Synchronously manipulating Zn²⁺ transfer and hydrogen/oxygen evolution kinetics in MXene host electrodes toward symmetric Zn-ions micro-supercapacitor with enhanced areal energy density. *Energy Storage Mater.* **2021**, *40*, 10–21. [[CrossRef](#)]
43. Yang, Q.; Huang, Z.; Li, X.; Liu, Z.; Li, H.; Liang, G.; Wang, D.; Huang, Q.; Zhang, S.; Chen, S.; et al. A wholly degradable, rechargeable Zn–Ti₃C₂ MXene capacitor with superior anti-self-discharge function. *ACS Nano* **2019**, *13*, 8275–8283. [[CrossRef](#)] [[PubMed](#)]
44. Li, L.; Zhang, D.; Deng, J.; Gou, Y.; Fang, J.; Cui, H.; Cao, M. Application of MXene-based materials in hybrid capacitor. *Sustain. Energy Fuels* **2021**, *5*, 3278–3291. [[CrossRef](#)]
45. Li, F.; Liu, Y.-l.; Wang, G.-G.; Zhang, S.-Y.; Zhao, D.-Q.; Fang, K.; Zhang, H.-Y.; Yang, H.Y. 3D porous H-Ti₃C₂T_x films as free-standing electrodes for zinc ion hybrid capacitors. *Chem. Eng. J.* **2022**, *435*, 135052. [[CrossRef](#)]
46. Mateen, A.; Ansari, M.Z.; Abbas, Q.; Muneeb, A.; Hussain, A.; Eldin, E.T.; Alzahrani, F.M.; Alsaiani, N.S.; Ali, S.; Javed, M.S. In Situ Nitrogen Functionalization of 2D-Ti₃C₂T_x-MXenes for High-Performance Zn-Ion Supercapacitor. *Molecules* **2022**, *27*, 7446. [[CrossRef](#)]
47. Gao, Z.W.; Zheng, W.; Lee, L.Y.S. Highly Enhanced Pseudocapacitive Performance of Vanadium-Doped MXenes in Neutral Electrolytes. *Small* **2019**, *15*, e1902649. [[CrossRef](#)]
48. Wickramaarachchi, K.; Minakshi, M.; Aravindh, S.A.; Dabare, R.; Gao, X.; Jiang, Z.-T.; Wong, K.W. Repurposing N-Doped Grape Marc for the Fabrication of Supercapacitors with Theoretical and Machine Learning Models. *Nanomaterials* **2022**, *12*, 1847. [[CrossRef](#)]
49. Jin, Y.; Ao, H.; Qi, K.; Zhang, X.; Liu, M.; Zhou, T.; Wang, S.; Xia, G.; Zhu, Y. A high-rate, long life, and anti-self-discharge aqueous N-doped Ti₃C₂/Zn hybrid capacitor. *Mater. Today Energy* **2021**, *19*, 100598. [[CrossRef](#)]
50. Fan, Z.; Jin, J.; Li, C.; Cai, J.; Wei, C.; Shao, Y.; Zou, G.; Sun, J. 3D-printed Zn-ion hybrid capacitor enabled by universal divalent cation-gelated additive-free Ti₃C₂ MXene ink. *ACS Nano* **2021**, *15*, 3098–3107. [[CrossRef](#)]
51. Mao, K.; Shi, J.; Zhang, Q.; Hou, Y.; Wen, L.; Liu, Z.; Long, F.; Niu, K.; Liu, N.; Long, F.; et al. High-capacitance MXene anode based on Zn-ion pre-intercalation strategy for degradable micro Zn-ion hybrid supercapacitors. *Nano Energy* **2022**, *103*, 107791. [[CrossRef](#)]
52. An, G.H.; Hong, J.; Pak, S.; Cho, Y.; Lee, S.; Hou, B.; Cha, S. 2D Metal Zn Nanostructure Electrodes for High-Performance Zn Ion Supercapacitors. *Adv. Energy Mater.* **2019**, *10*, 1902981. [[CrossRef](#)]

Disclaimer/Publisher’s Note: The statements, opinions and data contained in all publications are solely those of the individual author(s) and contributor(s) and not of MDPI and/or the editor(s). MDPI and/or the editor(s) disclaim responsibility for any injury to people or property resulting from any ideas, methods, instructions or products referred to in the content.